



Water flow induced piezoelectric polarization and sulfur vacancy boosting photocatalytic hydrogen peroxide evolution of cadmium sulfide nanorods

Yingge Zhang^{*}, Lingchao Wang^{*}, Hongwei Huang^{*}, Cheng Hu^{*}, Xiaolei Zhang^{*}, Chunyang Wang^{*}, Yihe Zhang^{*}

Engineering Research Center of Ministry of Education for Geological Carbon Storage and Low Carbon Utilization of Resources, Beijing Key Laboratory of Materials Utilization of Nonmetallic Minerals and Solid Wastes, National Laboratory of Mineral Materials, School of Materials Science and Technology, China University of Geosciences (Beijing), Beijing 100083, China

ARTICLE INFO

Keywords:

Water flow-driven
Defective CdS nanorods
Piezo-photocatalysis
H₂O₂ evolution
DFT calculations

ABSTRACT

Piezo-photocatalytic H₂O₂ production utilizing earth-abundant solar and mechanical energies, oxygen and water is a highly appealing route to produce renewable energy carriers. However, piezoelectric polarization always suffers from high-frequency mechanical vibration, which severely restricts its actual applications. Here, we report prominent piezo-photocatalytic H₂O₂ evolution from pure water triggered by low-frequency water flow induced mechanical stress over 1D CdS nanorods with sulfur vacancy (CdS NRs). The polar CdS NRs possess benign piezoelectric property and favorable morphology, enabling high sensitivity and respond to weak force of water flow, which contribute to yielding large piezoelectric polarization for photogenerated charges separation. Piezoelectric polarization also shows an inhibition effect on the photocorrosion of CdS to ·SO₃. Besides, DFT calculations demonstrate that sulfur vacancy allows enhanced O₂ adsorption and formation of the intermediate *OOH on the surface of CdS. Under simultaneous visible light and high-speed stirring, CdS NRs display a remarkably synergetic piezo-photocatalytic H₂O₂ production (1631.4 μmol g⁻¹ h⁻¹) without any sacrificial agents, 2.4 and 73.8 times of that under sole visible light and mechanical agitation, respectively. Importantly, it achieves an apparent quantum efficiency (AQY) of 1.32% at wavelength up to 500 nm and a solar-to-chemical (STC) conversion efficiency of 0.05% under one-sun illumination, which far exceeds other reported sulfide-based catalysts. This work integrates well with polarization engineering, defect engineering and morphology engineering to enhance catalytic behavior, providing a feasible strategy for designing efficient piezo-photocatalysts sensitive to weak mechanical forces.

1. Introduction

Hydrogen peroxide (H₂O₂), which is known as an efficient and green oxidant, has captured enormous attention since it was first synthesized in 1818 [1–3]. H₂O₂ is extensively used in fuel cells [4], chemical synthesis, environmental remediation, and medicine [5], etc. To date, the traditional anthraquinone technique for producing H₂O₂ is generally subjected to high energy consumption and pollution [6,7]. Fortunately, photocatalysis has emerged as a novel and sustainable technique for H₂O₂ production in recent years. And photocatalytic H₂O₂ production is expected to be a promising strategy to alleviate the energy crisis and the environmental pollution in terms of utilizing clean solar energy and producing pollution-free products. For example, Liu and coworkers [8] designed CoOx/Mo:BiVO₄/Pd system for the artificial photosynthesis of

H₂O₂, which can not only resist radical oxidation, but also deliver an appealing overall H₂O₂ photosynthesis efficiency among inorganic photocatalysts. Concretely, CoO_x/Mo:BiVO₄/Pd shows an AQY of 5.8% at 420 nm and a solar-to-chemical conversion (SCC) efficiency of 0.29% at full spectrum, as well as a H₂O₂ yield rate of 1425 μM/h in the absence of sacrificial agent.

Although the application of photocatalysis technology for H₂O₂ production has become a hot topic in recent years, however, the low separation efficiency of photogenerated electrons (e⁻) and holes (h⁺) hinders its practical application. Up to now, various strategies have been investigated to boost photocatalytic efficiencies, including bandgap engineering [9], defect engineering [10], cocatalysts [11], and heterojunction engineering [12]. Nevertheless, the single strategy is usually subjected to limited improvement effect. Encouragingly, researchers

^{*} Corresponding authors.

E-mail addresses: hwh@cugb.edu.cn (H. Huang), zyh@cugb.edu.cn (Y. Zhang).

<https://doi.org/10.1016/j.apcatb.2023.122714>

Received 15 December 2022; Received in revised form 26 February 2023; Accepted 30 March 2023

Available online 31 March 2023

0926-3373/© 2023 Elsevier B.V. All rights reserved.

have put forward the concept of a piezoelectric optoelectronic effect based on the synergy of semiconductors, piezoelectric properties, and light excitation [13,14]. It takes advantage of the energy derived from the surrounding environment (e.g., wave/water flow, vibration, and human movement, etc.) to trigger the generation of the polarization electric field, and break the shielding effect of photogenerated e^- and h^+ under a built-in electric field [15,16], and then to adjust the separation of the intrinsic free electron-hole (e^-h^+) pairs of catalyst to propel the redox reactions.

Generally, piezoelectric is a category of non-centrosymmetric materials that generate voltage when they are imposed by mechanical stress [17]. The piezo-potential induced by periodic mechanical energy supplies a driving force for the migration and separation of photo-generated charge carriers. Currently, varieties of piezoelectric semiconductors, e.g., BaTiO₃ [18], ZnO [19], ZnSnO₃ [20], NaNbO₃ [21], g-C₃N₄ [22], and CdS [23] have been widely developed. Particularly, CdS is a typical n-type semiconductor, which not only can be utilized in photocatalytic domains due to its suitable band gap (2.4 eV), good charge transfer ability, and visible light absorption capacity, but also can be applied to piezocatalytic fields owing to its asymmetry structure of wurtzite-structured CdS crystals. In general, the CdS crystal can be classified into two types of structures: sphalerite and wurtzite. The sphalerite-structured CdS crystal has good symmetry, and belongs to the T_d^2-F43m space group. The wurtzite-structured CdS crystal possess an asymmetric structure, corresponding to the $C_{6v}^4-P6_3mc$ space group and 6 mm point group, with cell parameters of $A=B=4.141$ Å, $C=6.720$ Å, which implies the piezoelectric characteristics of wurtzite-structured CdS. With the exclusive characteristics, wurtzite-structured CdS holds huge promise in the photocatalytic and piezocatalytic fields [24]. For instance, Zhang and co-workers [25] have fabricated the CdS phase junction for piezo-photocatalytic H₂ production. They found that phase junction within CdS contributes to improving structural asymmetry and inducing enhanced macroscopic polarization of wurtzite-structured CdS, which is favorable for the efficient separation of photogenerated carriers in piezo-photocatalysis. Nevertheless, current studies for constructing piezoelectric fields always involve high-frequency ultrasonic waves, which greatly impedes their industrial application. Hence, it is of remarkably practical significance to design piezo-photocatalysts that can actively capture discrete mechanical energy in the environment (e.g., water flow mechanical energy).

Aside from promoting carrier separation efficiency, increasing oxygen adsorption to expedite the oxygen reduction reaction (ORR) process is also a key factor to improve H₂O₂ yield. Therefore, defect engineering is introduced on the basis of the above regulation strategy to focus on tuning electronic structures and enriching active/adsorption sites. Up to now, studies on the application of CdS with defects in piezo-photocatalysis are rare. Hence, the realization of a prominently promoted H₂O₂ production through utilizing piezo-photocatalytic semiconductor combined with defect engineering will be of extensive research significance in the emerging field.

Enlightened by the above analysis, we designed CdS nanorods (NRs) with sulfur vacancy (Sv) via a one-step solvothermal reaction. The water flow as soft mechanical stress-induced piezoelectric field contributes to separating the photoinduced e^-h^+ pairs of CdS NRs, thus achieving a synergistic effect between photocatalysis and piezocatalysis. Meanwhile, moderate Sv of CdS NRs could not only act as active sites and trapping centers for photoinduced carriers, facilitating their transfer and separation, but also promote the oxygen adsorption capacity of CdS NRs. The realization of superior piezo-photocatalytic performance under low-frequency piezoelectric action and visible light is conducive to reducing energy consumption for better practical applications. Theoretical calculations further reveal that the piezoelectric potential on the surface of the catalyst increases with the increase of external force, and the O₂ adsorption energy of CdS-Sv under electric field along different axis directions are much smaller than that of CdS with perfect crystal

structure. This work points to the significance of low-frequency piezoelectric effect and defect engineering in enhancing photocatalytic H₂O₂ evolution activity, which shall provide a feasible guidance to excavate and design integrated defect and piezo-photocatalytic materials applied in a natural environment.

2. Results and discussions

2.1. Catalysts characterization

X-ray diffraction (XRD) patterns of the CdS NRs and CdS nanoparticles (CdS NPs) in Fig. 1a indicate that all diffraction peaks well correspond to the standard hexagonal CdS (JCPDS No.41-1049) with a space group of $P6_3mc$ (186) [25]. There is no difference in the peak position of the two samples, except for the change in peak intensity. Obviously, the content of the crystal plane (101) is higher than others in CdS NRs, while for CdS NPs, the content of the crystal plane (002) is the largest. The chemical states and surface elements of CdS NRs and CdS NPs were analyzed by X-ray photoelectron spectroscopy (XPS) measurement. As shown in Fig. 1b, the survey spectrum manifests the existence of Cd and S elements in CdS. The high-resolution XPS spectrum of Cd 3d emerges two typical peaks at 405.17 eV (Cd 3d_{5/2}) and 412.01 eV (Cd 3d_{3/2}) for CdS NPs (Fig. 1c), and they appear to shift towards lower binding energies for CdS NRs (405.03 eV and 411.78 eV), which can be attributed to the higher Sv concentration in CdS NRs [26, 27]. A similar phenomenon can be observed in the high-resolution XPS spectrum of S 2p. Specifically, two representative peaks of S 2p spectrum at 161.56 eV and 162.74 eV for CdS NPs and 161.53 eV and 162.80 eV for CdS NRs, corresponding to S 2p_{3/2} and S 2p_{1/2} of S²⁻ in CdS, respectively (Fig. 1d). In addition, the electron paramagnetic resonance (EPR) spectra in Fig. S1 also provide intuitive evidence for the existence of Sv. The strong signal response at $g = 2.003$ discloses that the Sv exists in both samples. Remarkably, the Sv signal intensity of CdS NRs is higher than that of CdS NPs, implying the higher concentration of Sv in CdS NRs. Subsequently, N₂ adsorption/desorption measurement was conducted to investigate the specific surface area and pore size distribution of CdS. As illustrated in Fig. 1e, the N₂ sorption isotherms of CdS NRs and CdS NPs are classified as type IV isotherms, which indicate that there are mesopores (2–50 nm) within the samples. The shape of hysteresis loops of the CdS NPs and CdS NRs is of type H2 and H3, respectively. As listed in Table S1, the BET surface area of CdS NRs is calculated to be 27.9 m² g⁻¹, which is almost 5.2-fold of CdS NPs (5.4 m² g⁻¹), and the pore size distributions inset Fig. 1e manifest the average pore diameters are 14.4 and 16.1 nm for CdS NPs and CdS NRs, respectively. This further certifies that CdS NRs are more favorable for piezo-photocatalytic H₂O₂ production as they could supply sufficient adsorption sites and efficient transport pathways [28]. The field emission scanning electron microscope (FESEM) image (Fig. 1f) reveals that the CdS NPs show an irregular spherical morphology formed by agglomerated nanoparticles, differing from the as-fabricated CdS NRs with a 1D rod-shaped morphology (Fig. 1g). In addition, the transmission electron microscope (TEM) image in Fig. 1h uncovers the rod-like, uniform, and smooth morphology of CdS NRs. Additionally, the high-resolution transmission electron microscope (HRTEM) image in Fig. 1i discloses that the interplanar distance of CdS NRs is 0.35 nm, which can be indexed to the (100) plane of wurtzite CdS. And the elemental mappings (Fig. 1j-l) manifest that Cd and S elements are dispersed homogeneously in CdS NRs.

2.2. Piezo-photocatalytic H₂O₂ evolution

The catalytic performance for H₂O₂ production of CdS is investigated under different conditions. As illustrated in Fig. 2a, CdS NRs shows a H₂O₂ yield rate of 695.3 μmol g⁻¹ h⁻¹ under visible light with low-speed stirring (LSS, 70 r/min). In contrast, the H₂O₂ production rate of CdS NRs is 22.1 μmol g⁻¹ h⁻¹ under sole high-speed stirring (HSS, 800 r/

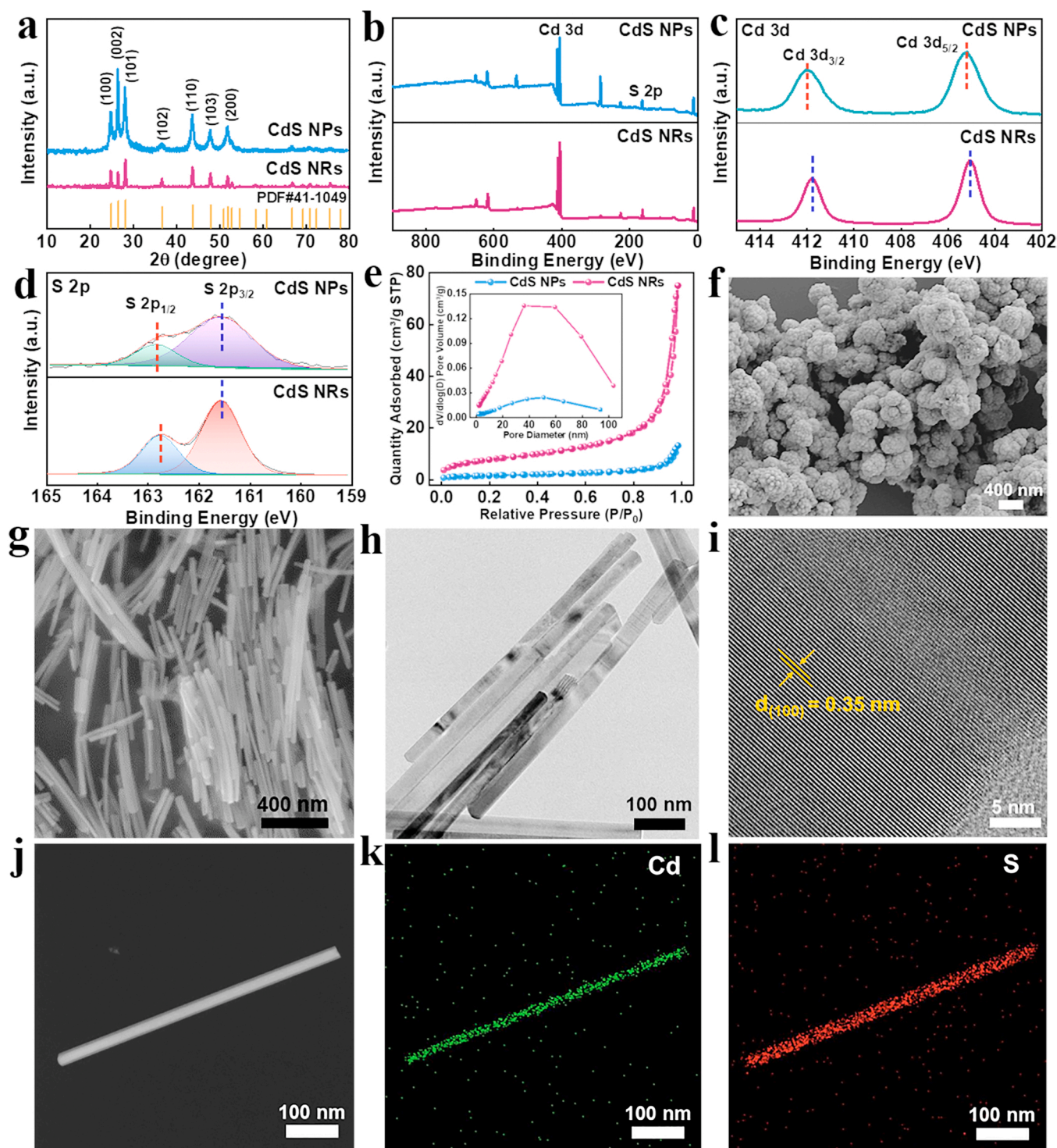


Fig. 1. (a) XRD patterns and (b) XPS survey spectra, (c) high-resolution XPS spectra of Cd 3d and (d) S 2p, and (e) Nitrogen adsorption-desorption isotherms and the corresponding pore size distribution curves (inset) of CdS NPs and CdS NRs. SEM images of (f) CdS NPs and (g) CdS NRs. (h) TEM image and (i) HRTEM image of CdS NRs. (j-l) Element mapping images of CdS NRs.

min). Notably, the photocatalytic H_2O_2 evolution rate increases to $1631.4 \mu\text{mol g}^{-1} \text{h}^{-1}$ under the combination of visible light and high-speed stirring (L+HSS). Besides, slight H_2O_2 is obtained without catalyst ($4.3 \mu\text{mol g}^{-1} \text{h}^{-1}$), which demonstrates the neglectable H_2O_2 self-production. It can be observed in Fig. 2b that the H_2O_2 evolution rate of CdS NRs is 32.2-fold that of CdS NPs ($50.6 \mu\text{mol g}^{-1} \text{h}^{-1}$) under the same irradiation conditions. The superior performance of CdS NRs can be ascribed to the larger piezoelectric response rendering efficaciously

photogenerated charge separation efficiency and abundant Sv enhancing the oxygen adsorption capacity. It is worth mentioning that piezo-photocatalytic H_2O_2 evolution rate is remarkably higher than the total sum of those in sole photocatalysis and piezocatalysis, indicating that mechanical force and light can synergistically elevate H_2O_2 production of CdS NRs. The reason can be assigned to that the e^- exchange between piezoelectric charges and the electroactive species would be boosted with the simultaneous agitator and light, which would enable

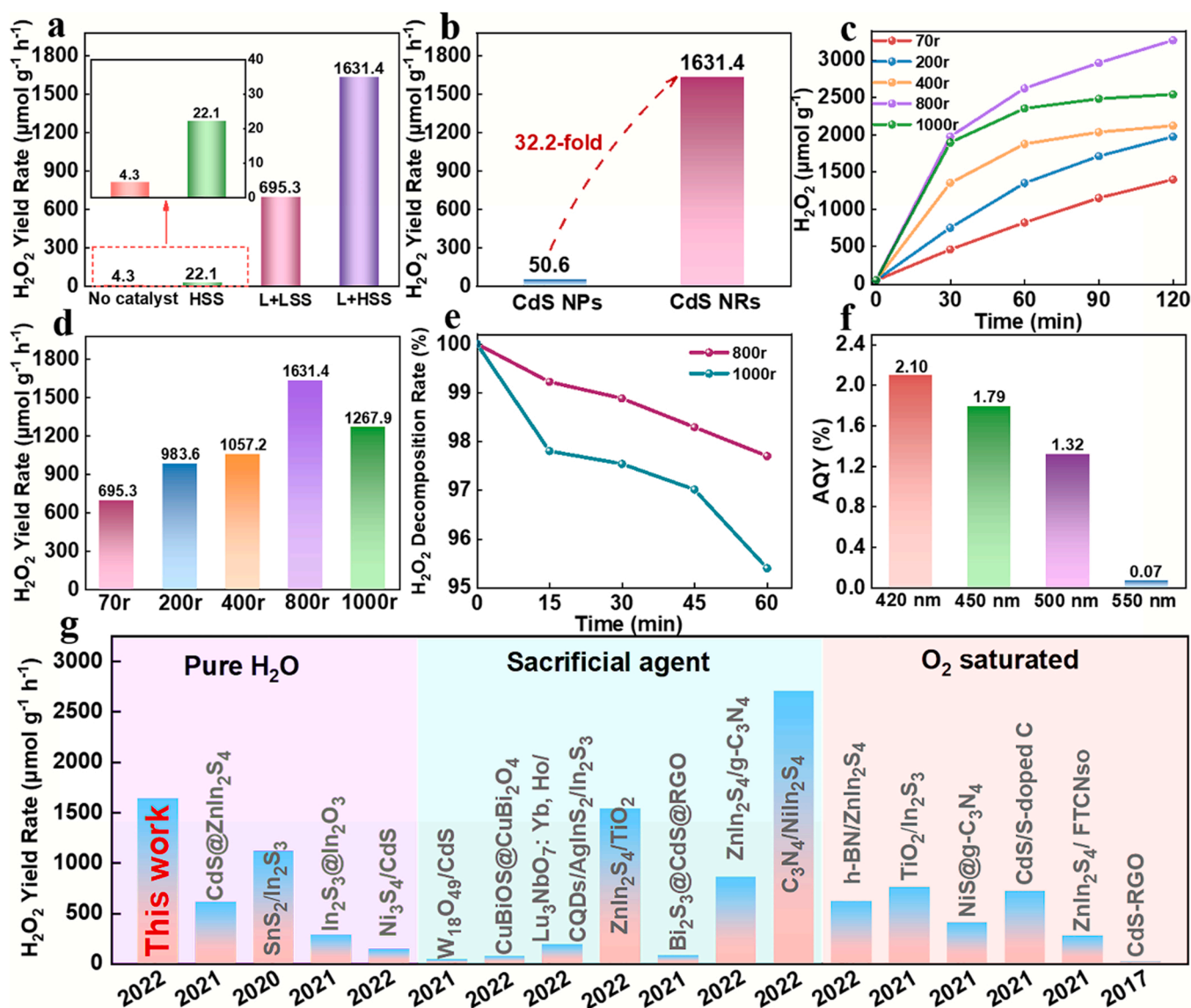


Fig. 2. (a) Catalytic H_2O_2 yield under no catalyst, high speed stirring (HSS), light and low speed stirring (L+LSS) and light and high-speed stirring (L+HSS) conditions. (b) Piezo-photocatalytic H_2O_2 yield of CdS NPs and CdS NRs at 800 r. (c) and (d) Piezo-photocatalytic H_2O_2 evolution rates of CdS NRs at 800 r and 1000 r. (e) Wavelength-dependent AQY for piezo-photocatalytic H_2O_2 evolution by CdS NRs. (f) Comparison of H_2O_2 production performance of CdS-based catalysts and other metal sulfides-based catalysts in recent years.

more energized surface charges to participate in the ORR before the appearance of an opposite direction piezoelectric field (Ep) [29].

For further confirmation, a systematic investigation of the influence of external force with different intensities on photocatalytic H_2O_2 production was carried out. As depicted in Fig. 2c and d, the experimental results reveal that the piezo-photocatalytic H_2O_2 evolution rates of CdS NRs exhibit a linearly increasing relationship with the stirring speed (<800 r). Specifically, the H_2O_2 yield rate is $695.3 \mu\text{mol g}^{-1} \text{h}^{-1}$ for 70 r, $983.6 \mu\text{mol g}^{-1} \text{h}^{-1}$ for 200 r, $1057.2 \mu\text{mol g}^{-1} \text{h}^{-1}$ for 400 r and $1631.4 \mu\text{mol g}^{-1} \text{h}^{-1}$ for 800 r, respectively. However, piezo-photocatalytic H_2O_2 yield of CdS NRs decreases at 1000 r ($1267.9 \mu\text{mol g}^{-1} \text{h}^{-1}$), which can be ascribed to the faster decomposition of H_2O_2 at 1000 r due to excessive rotational speed, as reflected by Fig. 2e. Additionally, AQY under the irradiation of monochromatic light was performed to determine the efficiency of light utilization of CdS NRs in pure water. As can be seen in Fig. 2f, the CdS NRs display high AQYs in visible light range, which still reaches 1.32% at 500 nm (Table S2). Similarly, the solar-to-chemical conversion efficiency of 0.05% is obtained under one-sun illumination (Table S3). To evaluate the stability of the catalyst, the

cycle performance, XRD and XPS tests after the cycles of CdS NRs were performed. As illustrated in Fig. S2a that CdS NRs exhibit a high initial piezo-photocatalytic H_2O_2 production of $3262.8 \mu\text{mol g}^{-1}$. However, the H_2O_2 evolution rate shows some decay in cycling process. This can be attributed to that the photocorrosion by holes and in situ over etching of the produced H_2O_2 , which can do some damage to the structure of CdS NRs. Encouragingly, the H_2O_2 production can still reach $2067.1 \mu\text{mol g}^{-1}$ after 3 cycles. Moreover, as can be observed in Fig. S2b that the shape and position of peaks in CdS NRs are almost unchanged, which indicates that the samples have a relatively good structural stability. However, the high resolution XPS spectrum of CdS NRs has undergone some obvious changes after piezo-photocatalytic H_2O_2 evolution. More specifically, in Fig. S2c, the Cd 3d spectrum of CdS NRs before the reaction presents two typical peaks at 405.03 eV and 411.78 eV, corresponding to Cd 3d_{5/2} and Cd 3d_{3/2}, respectively. The Cd 3d spectrum of CdS NRs after the reaction appears a slight shift to lower binding energies (404.86 eV and 411.60 eV) in contrast to that before the reaction. This phenomenon can also be observed in S 2p spectrum of CdS NRs before and after the reaction (Fig. S2d). Concretely, the binding energy

of S $2p_{3/2}$ centered at 161.53 eV has shifted to 161.35 eV, and S $2p_{1/2}$ located in 162.80 eV has moved to 162.50 eV. This can be attributed to the increased Sv of CdS NRs due to low-coordination S, which is generated due to the in situ etching by the continuous produced H_2O_2 during the piezo-photocatalytic reaction process [26,30]. There emerges a new peak at 168.69 eV in S 2p spectrum of CdS NRs after reaction compared to that before reaction, which can be assigned to the SO_3^-/SO_4^{2-} derived by the oxidized sulfur species [31–33]. However, the area of the new peak is relatively small, suggesting that the sulfur species are less oxidized. In conclusion, there are slight changes in the surface composition after the reaction, but they may do harm to the activity of the catalyst. To investigate the significant role of dissolved oxygen to the generation of H_2O_2 , piezo-photocatalytic H_2O_2 evolution test of CdS NRs was performed under Ar, air, and O_2 atmospheres, respectively. As can be observed in Fig. S3, the yields of H_2O_2 under air and O_2 atmosphere are remarkably higher than that of at an Ar atmosphere, implying the necessity of O_2 as reactant. Additionally, the production of H_2O_2 in an atmosphere of pure O_2 is even higher than that in that of air, further manifesting that dissolved oxygen content is crucial to the generation of H_2O_2 during the ORR process [34]. The piezo-photocatalytic H_2 evolution test was conducted to verify the high selectivity of CdS NRs in H_2O_2 production. As depicted in Fig. S4, CdS NRs show almost no photocatalytic H_2 activity in air and open environment. This can be attributed to that O_2 is easier to be reduced than H_2O by photogenerated electrons to produce $\cdot O_2$ and further to H_2O_2 . The photocatalytic H_2 production generally requires highly-pure inert atmosphere (N_2 or Ar), cocatalyst and large activation energy. Therefore, the reaction conditions for H_2O_2 generation are not favorable for H_2 evolution, suggesting that the high selectivity of CdS NRs in H_2O_2 evolution. Furthermore, the performance comparison of the photocatalytic, piezocatalytic, piezo-photocatalytic H_2O_2 evolution between CdS NRs and CdS-based or other sulfide catalysts is graphically shown in Fig. 2g. The comparison results manifest that the performance of CdS NRs far exceeds those of the reported catalysts.

2.3. Mechanism of piezo-enhanced photocatalysis

The piezoelectricity of CdS NRs and CdS NPs can be deduced from the phase curve and the butterfly amplitude loop measured on piezo-response force microscopy (PFM) (Fig. 3a and b). The large slope of the hysteresis loop indicates the strong piezoelectric polarization of catalyst. Fig. 3c shows the slope of the amplitude loop over CdS NRs and CdS NPs. It can be observed that CdS NRs possess a relatively stronger piezoelectric response compared with CdS NPs. It should be mentioned that the piezoelectricity of CdS NRs can create more polarization charges with the applied external stress, which is positively correlated with the piezoelectric potential and the piezo-photocatalytic H_2O_2 production performance (Fig. 3f). Moreover, COMSOL calculation is carried out to further unveil the significant role of the morphology on the piezoelectric response ability. The simulation model is established based on the size and morphology characteristics of CdS NPs and CdS NRs from Fig. 1f and g [35]. The results discover that the surface piezoelectric potential of the CdS NRs is larger than that of CdS NPs (Fig. 3d and e), and the piezoelectric potential of CdS NRs is augmented with increasing applied external force (Figs. S5). The bigger piezoelectric potential of CdS NRs contributes to better charge separation/transportation efficiency, leading to promoted piezo-photocatalytic H_2O_2 performance.

To investigate charge transfer under different conditions, the photocurrent responses of CdS NRs under HSS, L, and L+HSS were carried out (Fig. 4a–f). As displayed in Fig. 4a and b, the CdS NRs exhibit weak piezocurrent response when HSS is applied. In comparison, CdS NRs deliver a much stronger photocurrent response when visible light is given (Fig. 4c and d). Subsequently, to gain a deeper understanding on the relationship between piezocatalysis and photocatalysis, the simultaneous HSS and light are exerted (Fig. 4e and f). Remarkably, the average piezophotocurrent of CdS NRs (60 μA) is increased by more than 30 times compared to that under HSS and about 2.40-fold of that under light, which indicates that the synergy of agitation and illumination contributes to boosting the charges separation efficiency of CdS NRs (Fig. 4g). In addition, the superior charge separation characteristic of CdS NRs was further confirmed by electrochemical impedance

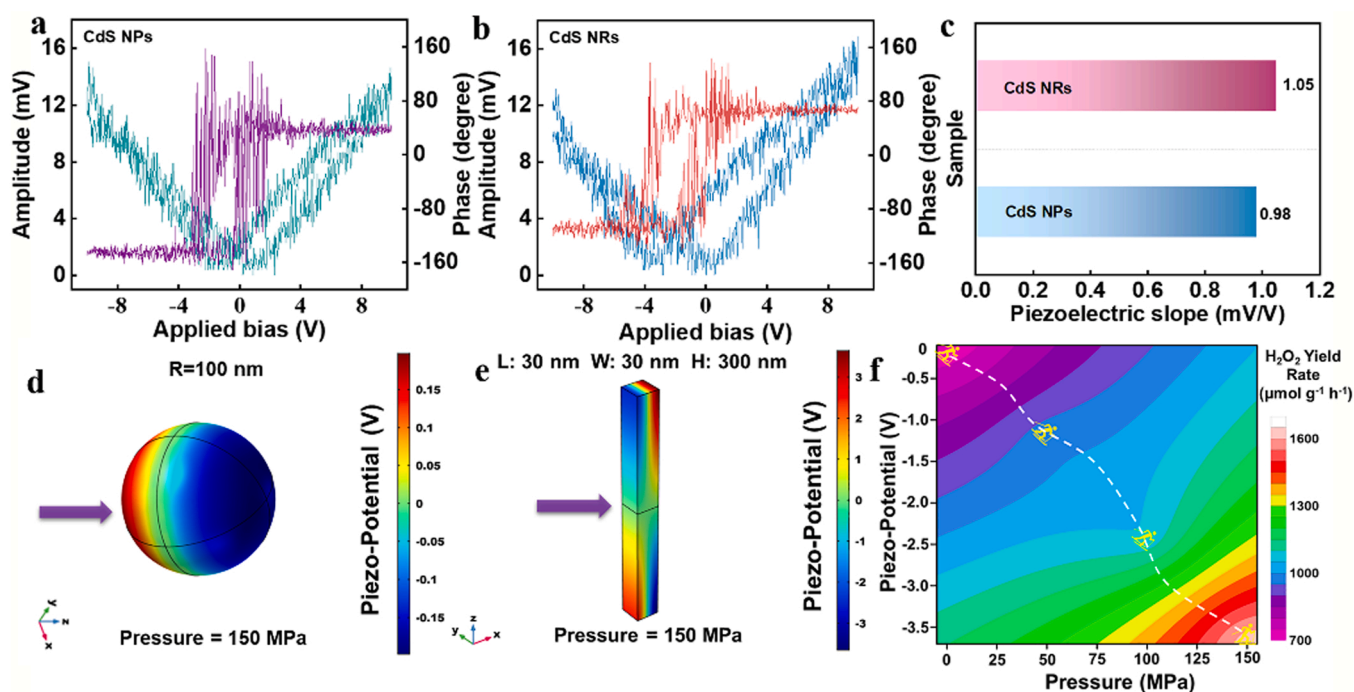


Fig. 3. Butterfly amplitude loop and phase curve of (a) CdS NPs and (b) CdS NRs. (c) The slope of the hysteresis loop over different samples. Theoretical calculations of the corresponding piezoelectric potential distribution induced on the surface of (d) CdS NPs and (e) CdS NRs at applied stress of 150 MPa. (f) Variation trend diagram of the piezo-potential and the H_2O_2 yield rate of CdS NRs.

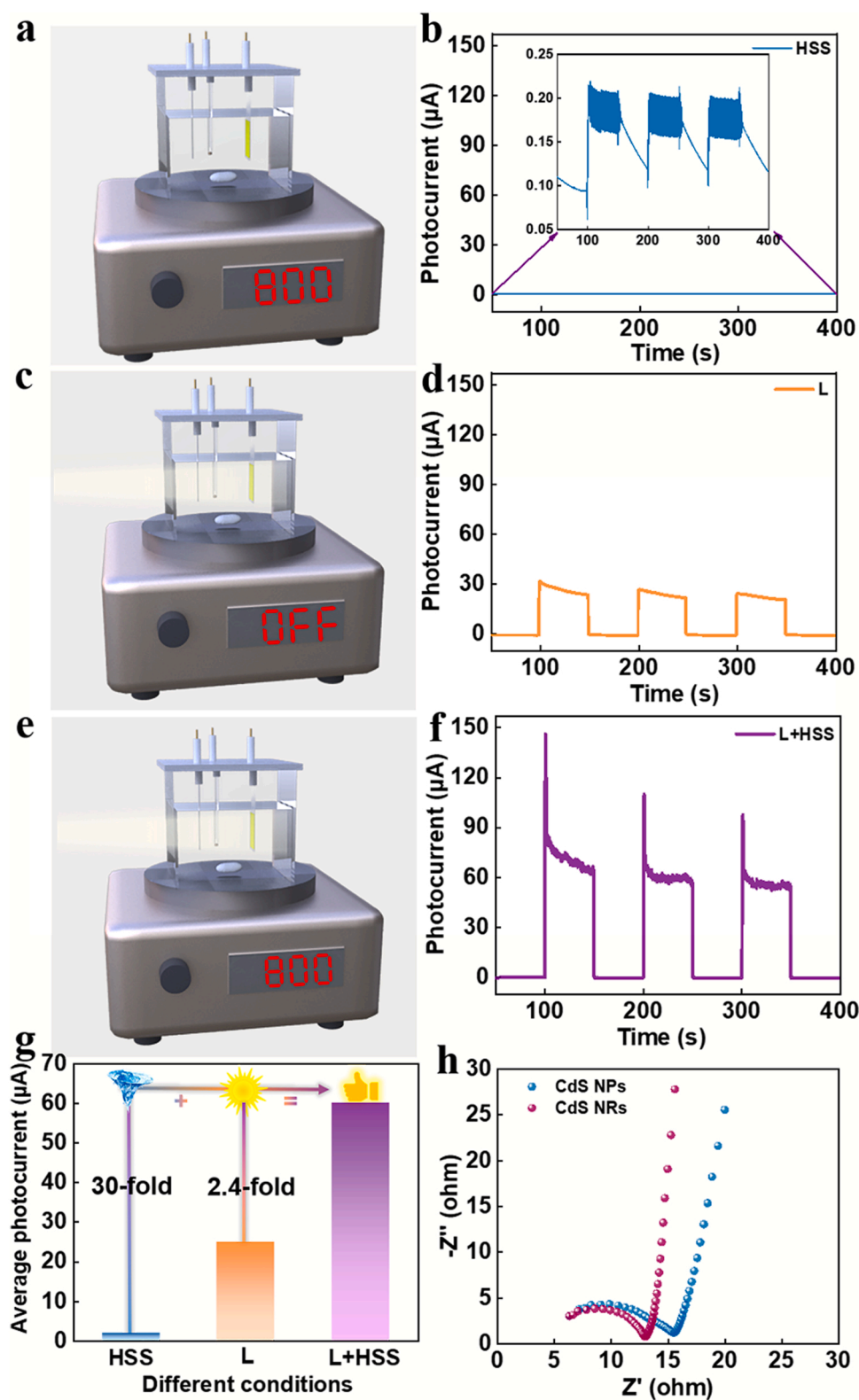


Fig. 4. Schematic diagram of the simulation of the photocurrent test under (a) HSS, (c) L, and (e) HSS+L. Current measured at 0 V versus Hg/Hg₂Cl₂ of CdS NRs under (b) HSS and (d) L, and (f) HSS +L conditions for CdS NRs. (g) Comparison of the average current of CdS NRs under different conditions. (h) EIS Nyquist plots.

spectroscopy (EIS) measurements. Specifically, the EIS Nyquist plots in Fig. 4h reveal that CdS NRs present a smaller arc radius in contrast to that of CdS NPs, illustrating a lower intrinsic resistance and faster transfer of photogenerated charge.

To investigate the charge-transfer behavior of CdS with perfect

crystal structure (marked as CdS) and CdS with Sv (marked as CdS-Sv), the charge difference of them is analyzed by Density Functional Theory (DFT) First Principle calculations. Apparently, the introduction of Sv reduces the number of S atoms that bond with Cd atoms in the lattice, which in turn renders a decrease in the degree of Cd 5 s orbital electrons

participating in bonding and an increase in the Cd 5 s orbital valence electron cloud density (Fig. 5a-c) compared to that of CdS (Figs. S6a-c) under the application of electric fields along different axis directions. As we know, O_2 is the main reactant in H_2O_2 production process. Therefore, exploring the adsorption capacity of the catalyst for O_2 will be conducive to understanding the feasibility of H_2O_2 production and catalytic activity of the catalyst. The charge difference of O_2 adsorbed in CdS-Sv and CdS are depicted in Fig. 5d-f and Figs. S6d-f, respectively. Obviously, there exists a strong charge interaction between O_2 and Sv. Moreover, the O_2 adsorption energy of CdS-Sv is significantly smaller than that of CdS under electric fields along different axis directions (Fig. 5g, Table S4, and Table S5), which indicates that the integration of Sv contributes to supplying more O_2 adsorption sites, leading to electrons of the Cd atomic valence shell being more easily captured by O_2 , and O_2 is more likely activated to engage in the ORR. In addition, the work function of CdS-Sv (Fig. 5h-j) is lower than that of CdS (Figs. S6g-i), which means that the Fermi level of defective CdS is higher and there will be more electrons transferred from the surface of defective CdS to

the solution to initiate the photocatalytic reaction.

The separation efficiency and diffusion rate of photogenerated charge carriers play a dominant role in deciding the photocatalytic performance of a semiconductor. In general, the mobility of photoinduced charge carriers is inversely proportional to their effective mass, which implies that a smaller effective mass enables the charge carriers to reach the surface reaction sites within their lifetime more easily, thus leading to enhanced catalytic activity. To probe the influence of piezoelectric polarization on the effective charge mass of electron (m_e) over CdS-Sv, DFT calculations on CdS and CdS-Sv under electric field along different axis directions are conducted. The m_e of CdS-Sv under electric field along c axis is relatively smaller than those under other electric field directions (Table S6), demonstrating that the photogenerated electrons of CdS-Sv under electric field along c axis is more prone to separate and transfer to the surface of the catalyst to participate in the reaction and thus inhibit the recombination of photogenerated e^- and h^+ pairs. This can be deduced from the effect of the internal electric field along the [0001] direction within CdS-Sv on photocatalytic activity

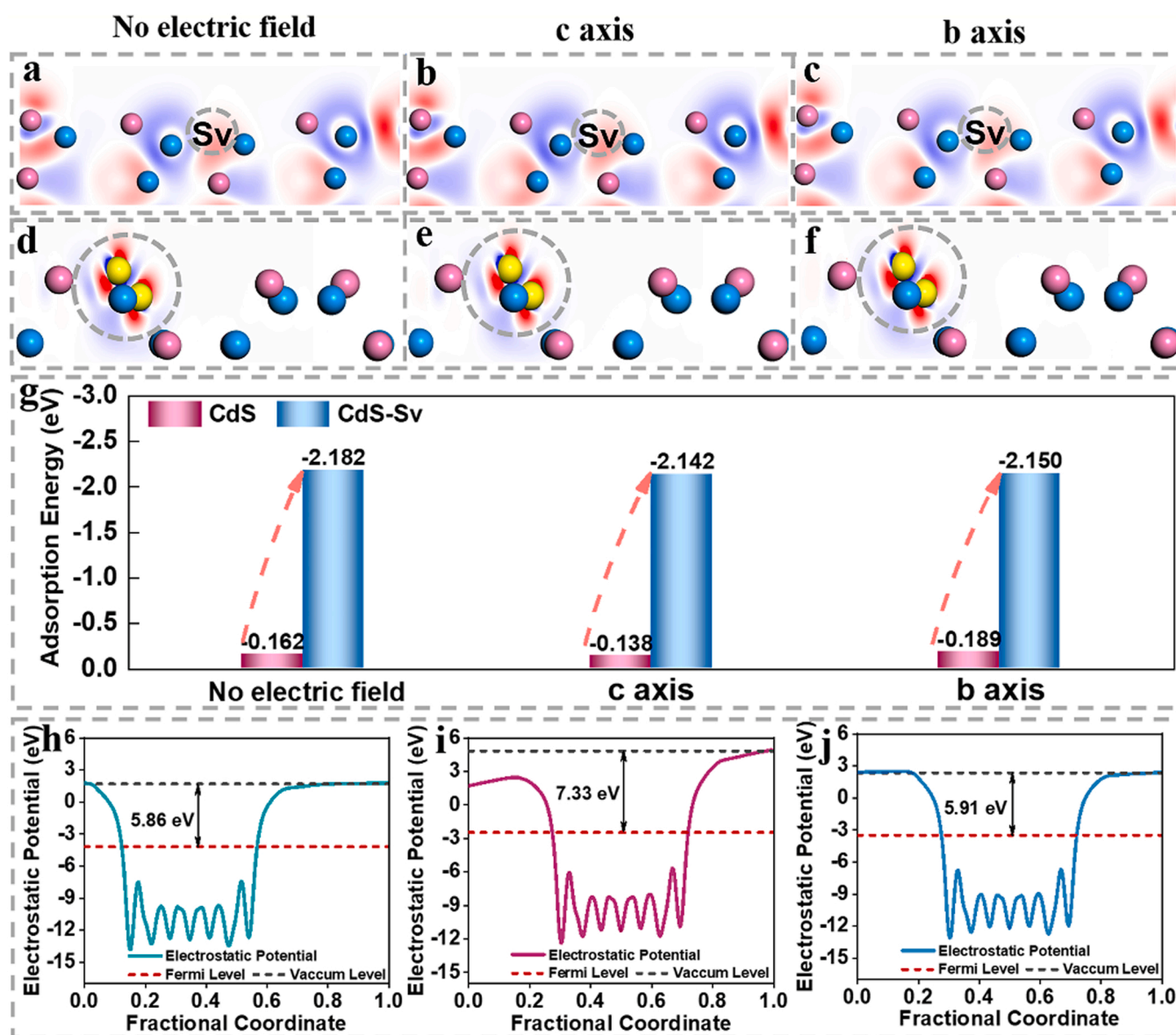


Fig. 5. Charge difference of CdS-Sv under (a) no electric field, electric field along c axis (b) and b axis (c). Charge difference of O_2 adsorbed on CdS-Sv under (d) no electric field, electric field along c axis (e) and b axis (f) (charge accumulation and depletion involve in the red and blue regions, respectively). (g) O_2 adsorption energy of CdS-Sv and CdS under electric field along different axis direction. Work function of CdS-Sv under (h) no electric field, electric field along c axis (i) and b axis (j).

[36]. Moreover, conclusion can also be reached that the changes in electronic structures caused by Sv manifest that the electron-donor species could act as a dopant to expedite the electron mobility.

To reveal the mechanism of photocatalytic reactions induced by the piezophototronic effect, the main free radicals in H_2O_2 production process were well investigated using electron spin resonance spectroscopy (ESR). In Fig. 6, it can be observed that $\bullet\text{O}_2^-$, $\bullet\text{OH}$ and $\bullet\text{SO}_3^-$ are generated by CdS NRs under HSS, L+LSS, and L+HSS. CdS NRs present the highest intensity of ESR affiliated with $\bullet\text{O}_2^-$ (Fig. 6c and d) and $\bullet\text{OH}$ (Fig. 6g and h) under L+HSS in contrast to that of the single HSS (Fig. 6b

and f, respectively) and L+LSS condition (Fig. 6a and e, respectively), demonstrating the largest number of $\bullet\text{O}_2^-$ and $\bullet\text{OH}$ under L+HSS. The results are also consistent with the piezo-photocatalytic H_2O_2 production performance of CdS NRs, which demonstrates that photocatalysis plays a dominant role in the evolution of H_2O_2 and piezoelectric polarization further facilitates the photocatalytic H_2O_2 evolution. Furthermore, it should be mentioned that $\bullet\text{OH}$ in the reaction are primary derived from a two-step ORR by piezo-photoexcited e^- according to Eqs. (1–4), which also verifies that O_2 takes a crucial part in the generation of H_2O_2 [37]. As a result of the introduction of Sv, the

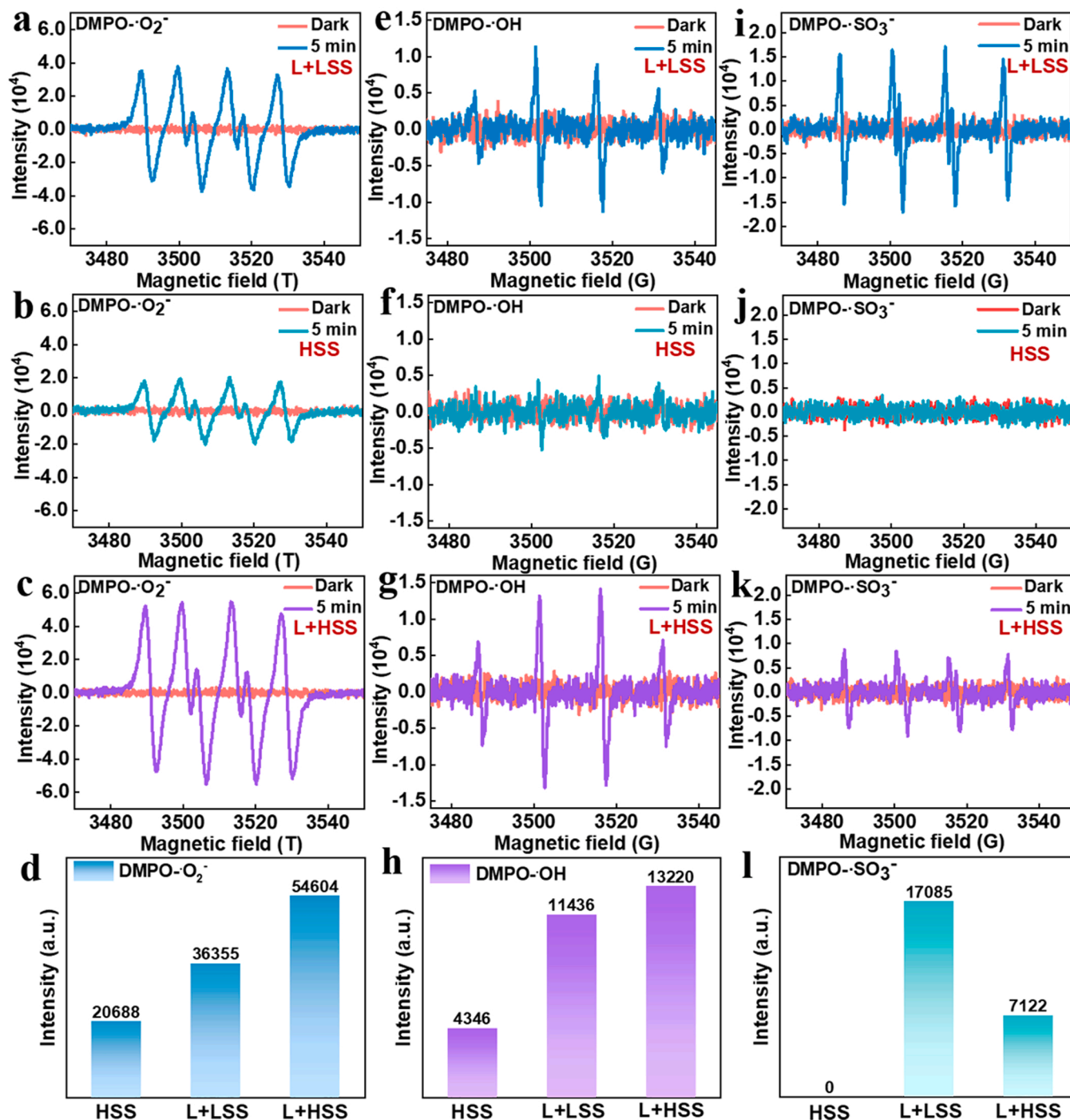


Fig. 6. ESR spectra of radical adducts trapped by DMPO- O_2^- in the dispersion of CdS NRs under (a) L+LSS, (b) HSS and (c) L+HSS for 5 min. ESR spectra of radical adducts trapped by DMPO- OH in the dispersion of CdS NRs under (e) L+LSS, (f) HSS and (g) L+HSS for 5 min. ESR spectra of radical adducts trapped by DMPO- SO_3^- in the dispersion of CdS NRs under (i) L+LSS, (j) HSS and (k) L+HSS for 5 min. (d, h and l) Comparison of ESR signal as an indicator for $\bullet\text{O}_2^-$, $\bullet\text{OH}$ and $\bullet\text{SO}_3^-$ relatively concentration of CdS NRs under different conditions.

as-prepared CdS NRs allow for the capture of more O_2 for ORR. Combining these advantages, the defective CdS NRs present excellent piezo-photocatalytic H_2O_2 activity through a $2e^-$ ORR process. In addition, to check whether the surface sulfur atoms of CdS NRs could be generated into the oxidizing sulfur species and investigate the effect of oxidizing sulfur species on the piezo-photocatalytic H_2O_2 activity of CdS, the ESR spectra of $\bullet SO_3$ trapped by DMPO in the dispersion of CdS NRs under different conditions were measured. Experimental results discover that there are oxidizing sulfur species formed in the reaction, which is also in accordance with the analysis of the high resolution XPS spectrum of S 2p. Concretely, the relative intensity of DMPO- $\bullet SO_3$ over CdS NRs under L+LSS (Fig. 6i and l) is higher than that of L+HSS

condition (Fig. 6k), implying that sulfur atoms in CdS NRs under L+LSS are more easily oxidized than that under L+HSS. Meanwhile, it can be well proved that the introduction of piezoelectric polarization can promote the rapid migration and separation of photogenerated charges in CdS NRs, allowing them to rapidly participate in the generation of H_2O_2 . Moreover, there is almost no $\bullet SO_3$ formation under HSS (Fig. 6j), implying that the photocorrosion of CdS is mainly caused by light irradiation, and the introduction of piezoelectric polarization can inhibit the photocorrosion to a certain extent.

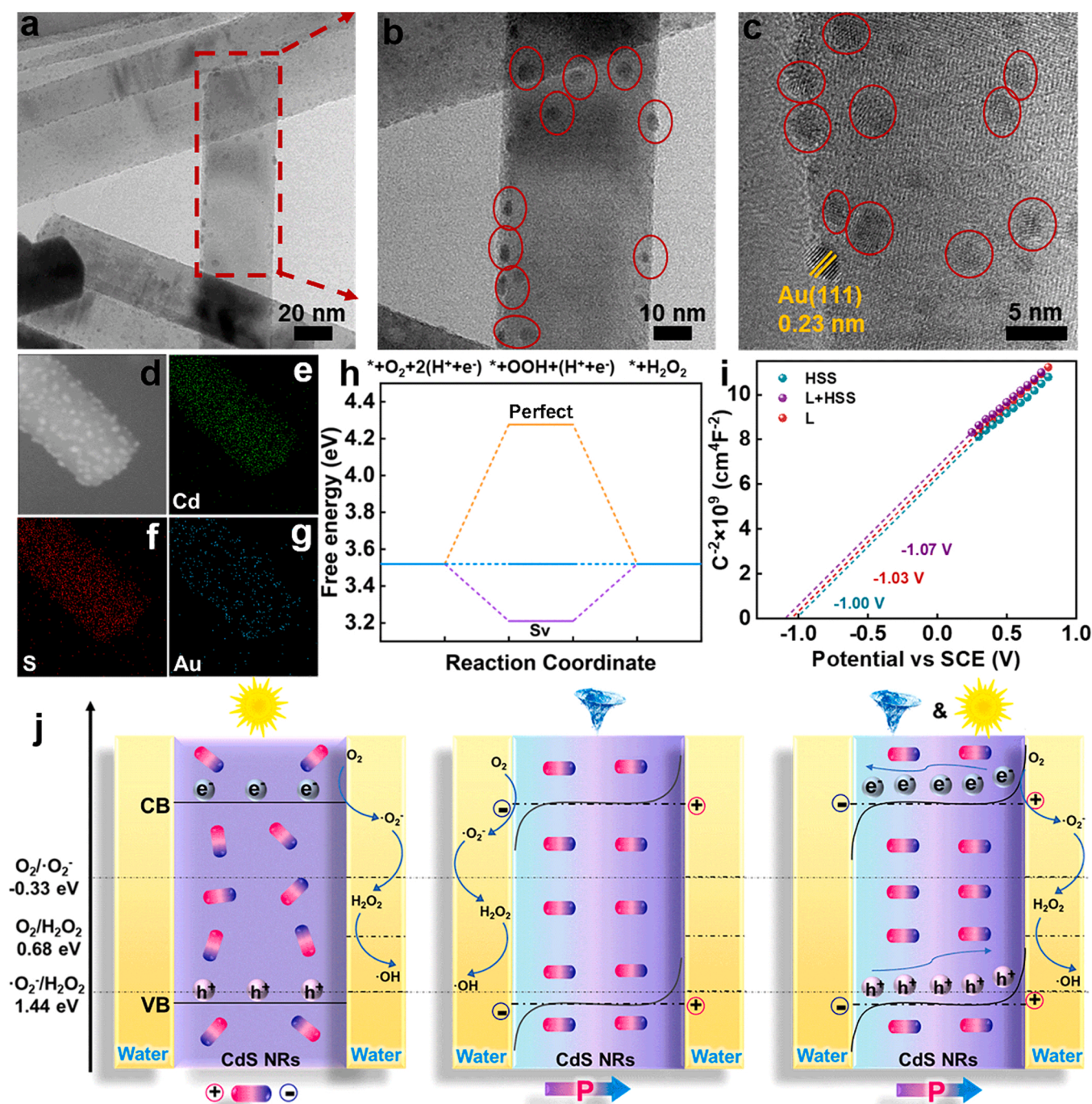


Fig. 7. (a-c) TEM and HRTEM images of CdS NRs after HSS and photodeposition with Au. (d-g) The element mapping of CdS NRs. (h) Free energy diagrams of $2e^-$ ORR on CdS NRs at $U = 0.7$ V versus RHE. (i) Mott-Schottky plots of CdS NRs under HSS, L, and L+HSS conditions. (j) The proposed charge transfer and reaction mechanism under HSS and light.



To gain a deep understanding of the locations of active reductive sites on CdS NRs, the deposition of Au with $\text{HAuCl}_4 \cdot 4\text{H}_2\text{O}$ as a precursor under piezo-photocatalytic conditions is carried out. Owing to the chaotic direction of the agitator applied to the nanorods, it can be inferred that the strain-induced reactive sites might reside in the whole nanorods. As expected, the experimental results in Fig. 7a-c demonstrate that the reduction active sites existed on the side and tip of CdS NRs. In particular, Fig. 7b and c reveal that Au quantum dots (QDs) are abundantly and uniformly deposited on the CdS NRs (the black spot marked by a red circle). Additionally, the lattice spacing of Au QDs in Fig. 7c is measured to be 0.23 nm, which corresponds to the (111) plane of Au (JCPDS card No. 04-0784) [38]. Furthermore, the element mapping images in Fig. 7d-g also provide direct evidence that Au QDs are successfully deposited on CdS NRs. Therefore, it can be concluded that the photo-enhanced surface charge migration and strain-induced surface-active sites synergistically result in superb H_2O_2 evolution activity of CdS NRs during the piezo-photocatalytic process. TPD- O_2 measurement was conducted to evaluate O_2 adsorption ability of CdS samples. As illustrated in Fig. S7a, the TPD- O_2 result shows that the CdS NRs possess stronger O_2 adsorption ability and O_2 surface binding strength than the CdS NPs, further confirming that higher Sv concentration is more beneficial for O_2 adsorption [39]. Then, TG-DSC measurement was carried out to investigate the mass loss and endothermic/exothermic rates of CdS samples with the change of temperature. As shown in Fig. S7b, a slight weight loss of $\sim 0.6\%$ for CdS NPs and $\sim 0.3\%$ for CdS NRs appear at around 250°C , which can be ascribed to the evaporation of absorbed water. From about 300°C , the obvious weight loss of CdS NPs and slight weight loss of CdS NRs can be attributed to the occurrence of oxidation reaction. Notably, CdS NRs show a less weight loss ratio than CdS NPs, which is in good accordance with the much stronger O_2 adsorption of CdS NRs as revealed in above TPD- O_2 profiles.

The enhancement of the adsorption properties of O_2 is favorable to facilitate the occurrence of ORR, resulting in supreme H_2O_2 evolution activity. Then DFT calculations were used to explore the fundamental steps of the 2e^- ORR process. Generally, for a perfect 2e^- ORR catalyst, $\bullet\text{OOH}$ adsorption ought to keep thermoneutrality under equilibrium potential ($U = 0.7\text{ V}$ versus reversible hydrogen electrode), which corresponds to the free energy of $\bullet\text{OOH}$ ($\sim 3.52\text{ eV}$) [40–42]. CdS with perfect catalyst structure exhibits relatively high O_2 activation barrier (Fig. 7 h), implying that the catalyst has a low 2e^- ORR catalytic activity but high selectivity compared to the ideal model and CdS-Sv. In addition, the latter inclines to be reduced to $\bullet\text{O}$ in next steps because of the stronger binding capability with $\bullet\text{OOH}$. To be more comprehensive, the distance between catalysts with the ideal model should be considered as a standard to evaluate the underlying catalytic performance of the catalyst [3]. Thus, it is concluded that CdS-Sv is more superior to CdS.

Based on the analysis presented above, the piezo-enhanced photocatalytic process can be illustrated in Fig. 7i and j. The Mott-Schottky (MS) curves (Fig. 7i) disclose that the flat band potential (E_{fb}) of CdS NRs with a frequency of 1000 Hz becomes more negative under L+HSS compared with those under L and HSS. The reason can be ascribed to that the deformed piezoelectric is subjected to an energy shift on the conduction band (CB) and valence band (VB) across the catalyst and generates a piezo-potential under stress, which drives the transfer of e^- from the VB of piezoelectric to substance in solution for H_2O_2 production. The E_{p} induced by water flow increases with increasing stirring speed due to stronger shear force, and light integration contributes to the exchange of e^- between piezoelectric charges and electroactive species, resulting in more effective energized surface charges to participate in the H_2O_2 production process (Fig. 7j) [29]. Therefore, the

conclusion can be drawn that the rapid charge transfer and suitable energy shift take a dominant role in kinetics of piezo-enhanced photocatalytic H_2O_2 evolution.

3. Conclusions

In summary, we fabricated defective CdS NRs via a simple solvothermal reaction. By designing the CdS piezo-photocatalyst with suitable morphology and Sv concentration, and harvesting ambient high-speed water flow and solar energy to achieve highly-efficient piezo-photocatalytic H_2O_2 production performance. The appropriate Sv in CdS NRs can behave as trapping centers and active sites for photoinduced charge carriers, as well as enhance the O_2 adsorption capacity and form the intermediate $\bullet\text{OOH}$ on the surface of CdS NRs. Importantly, the low-frequency water flow-induced piezoelectric polarization contributes to the photogenerated charge separation, thus leading to more available charge carriers participating in H_2O_2 yield process. With all these merits, the CdS NRs deliver a prominent synergetic piezo-photocatalytic H_2O_2 yield rate of $1631.4\text{ }\mu\text{mol g}^{-1}\text{ h}^{-1}$, significantly higher than that of sole water flow or visible light irradiation. This work opens a feasible door to co-utilize solar and mechanical energies for H_2O_2 production and sheds new light on exploring CdS-based polar materials as high-performance piezo-photocatalysts.

CRedit authorship contribution statement

Yingge Zhang: Conceptualization, Methodology, Investigation, Writing – original draft. **Lingchao Wang:** Methodology, Data curation. **Hongwei Huang:** Resources, Writing – review & editing, Data curation, Supervision. **Cheng Hu:** Methodology, Data curation. **Xiaolei Zhang:** Formal analysis, Writing – review & editing. **Chunyang Wang:** Formal analysis, Writing – review & editing. **Yihe Zhang:** Resources, Writing – review & editing, Supervision, Data curation.

Declaration of Competing Interest

The authors declare that they have no known competing financial interests or personal relationships that could have appeared to influence the work reported in this paper.

Data Availability

Data will be made available on request.

Acknowledgements

This work was jointly supported by the National Key Research and Development Program of China (2022YFB3803600). This work was also jointly supported by the National Natural Science Foundation of China (Nos. 52072347, 51572246, 52272244 and 51972288).

Appendix A. Supporting information

Supplementary data associated with this article can be found in the online version at doi:10.1016/j.apcatb.2023.122714.

References

- [1] H. Hou, X. Zeng, X. Zhang, Production of hydrogen peroxide by photocatalytic processes, *Angew. Chem. Int. Ed.* 59 (2020) 17356–17376.
- [2] J.M. Campos-Martin, G. Blanco-Brieva, J.L.G. Fierro, Hydrogen peroxide synthesis: an outlook beyond the anthraquinone process, *Angew. Chem. Int. Ed.* 45 (2006) 6962–6984.
- [3] J. Kang, X. Qiu, Q. Hu, J. Zhong, X. Gao, R. Huang, C. Wan, L.-M. Liu, X. Duan, L. Guo, Valence oscillation and dynamic active sites in monolayer NiCo hydroxides for water oxidation, *Nat. Catal.* 4 (2021) 1050–1058.
- [4] K. Mase, M. Yoneda, Y. Yamada, S. Fukuzumi, Seawater usable for production and consumption of hydrogen peroxide as a solar fuel, *Nat. Commun.* 7 (2016) 11470.

- [5] H. Song, L. Wei, L. Chen, H. Zhang, J. Su, Photocatalytic production of hydrogen peroxide over modified semiconductor materials: a minireview, *Top. Catal.* 63 (2020) 895–912.
- [6] Z. Teng, Q. Zhang, H. Yang, K. Kato, W. Yang, Y.-R. Lu, S. Liu, C. Wang, A. Yamakata, C. Su, B. Liu, T. Ohno, Atomically dispersed antimony on carbon nitride for the artificial photosynthesis of hydrogen peroxide, *Nat. Catal.* 4 (2021) 374–384.
- [7] S. Yang, A. Verdager-Casadevall, L. Arnarson, L. Silvio, V. Čolić, R. Frydendal, J. Rossmeisl, I. Chorkendorff, I.E.L. Stephens, Toward the decentralized electrochemical production of H_2O_2 : a focus on the catalysis, *ACS Catal.* 8 (2018) 4064–4081.
- [8] T. Liu, Z. Pan, J.J.M. Vequizo, K. Kato, B. Wu, A. Yamakata, K. Katayama, B. Chen, C. Chu, K. Domen, Overall photosynthesis of H_2O_2 by an inorganic semiconductor, *Nat. Commun.* 13 (2022) 1034.
- [9] Y. Zhong, Y. Shao, F. Ma, Y. Wu, B. Huang, X. Hao, Band-gap-matched CdSe QD/WS₂ nanosheet composite: Size-controlled photocatalyst for high-efficiency water splitting, *Nano Energy* 31 (2017) 84–89.
- [10] Y. Zhang, Y. Zhang, H. Zhang, L. Bai, L. Hao, T. Ma, H. Huang, Defect engineering in metal sulfides for energy conversion and storage, *Coord. Chem. Rev.* 448 (2021), 214147.
- [11] Y. Yang, Y. Zhang, Z. Fang, L. Zhang, Z. Zheng, Z. Wang, W. Feng, S. Weng, S. Zhang, P. Liu, Simultaneous realization of enhanced photoactivity and promoted photostability by multilayered MoS₂ coating on CdS nanowire structure via compact coating methodology, *ACS Appl. Mater. Interf.* 9 (2017) 6950–6958.
- [12] J. Zhang, Y. Wang, J. Jin, J. Zhang, Z. Lin, F. Huang, J. Yu, Efficient visible-light photocatalytic hydrogen evolution and enhanced photostability of core/shell CdS/g-C₃N₄ nanowires, *ACS Appl. Mater. Interf.* 5 (2013) 10317–10324.
- [13] C. Hu, H. Huang, F. Chen, Y. Zhang, H. Yu, T. Ma, Coupling piezocatalysis and photocatalysis in Bi₄NbO₈X (X = Cl, Br) polar single crystals, *Adv. Funct. Mater.* 30 (2020), 1908168.
- [14] S. Lin, S. Li, H. Huang, H. Yu, Y. Zhang, Synergetic piezo-photocatalytic hydrogen evolution on Cd_{1-x}Zn_xS solid-solution 1D nanorods, *Small* 18 (2022), 2106420.
- [15] D. You, L. Liu, Z. Yang, X. Xing, K. Li, W. Mai, T. Guo, G. Xiao, C. Xu, Polarization-induced internal electric field to manipulate piezo-photocatalytic and ferro-photoelectrochemical performance in bismuth ferrite nanofibers, *Nano Energy* 93 (2022), 106852.
- [16] F. Chen, H. Huang, L. Guo, Y. Zhang, T. Ma, The role of polarization in photocatalysis, *Angew. Chem. Int. Ed.* 58 (2019) 10061–10073.
- [17] C. Hu, S. Tu, N. Tian, T. Ma, Y. Zhang, H. Huang, Photocatalysis enhanced by external fields, *Angew. Chem. Int. Ed.* 60 (2021) 16309–16328.
- [18] X. Zhou, S. Wu, C. Li, F. Yan, H. Bai, B. Shen, H. Zeng, J. Zhai, Piezophototronic effect in enhancing charge carrier separation and transfer in ZnO/BaTiO₃ heterostructures for high-efficiency catalytic oxidation, *Nano Energy* 66 (2019), 104127.
- [19] Z. Wang, T. Hu, H. He, Y. Fu, X. Zhang, J. Sun, L. Xing, B. Liu, Y. Zhang, X. Xue, Enhanced H₂ production of TiO₂/ZnO nanowires Co-Using solar and mechanical energy through piezo-photocatalytic effect, *ACS Sustain. Chem. Eng.* 6 (2018) 10162–10172.
- [20] M.-K. Lo, S.-Y. Lee, K.-S. Chang, Study of ZnSnO₃-nanowire piezophotocatalyst using two-step hydrothermal synthesis, *J. Phys. Chem. C* 119 (2015) 5218–5224.
- [21] S. Singh, N. Khare, Coupling of piezoelectric, semiconducting and photoexcitation properties in NaNbO₃ nanostructures for controlling electrical transport: Realizing an efficient piezo-photoanode and piezo-photocatalyst, *Nano Energy* 38 (2017) 335–341.
- [22] C. Hu, J. Hu, Z. Zhu, Y. Lu, S. Chu, T. Ma, Y. Zhang, H. Huang, Orthogonal charge transfer by precise positioning of silver single atoms and clusters on carbon nitride for efficient piezocatalytic pure water splitting, *Angew. Chem. Int. Ed.* 61 (2022), e202212397.
- [23] Y.-F. Lin, J. Song, Y. Ding, S.-Y. Lu, Z.L. Wang, Alternating the output of a CdS nanowire nanogenerator by a white-light-stimulated optoelectronic effect, *Adv. Mater.* 20 (2008) 3127–3130.
- [24] Y. Zhao, Z.-B. Fang, W. Feng, K. Wang, X. Huang, P. Liu, Hydrogen production from pure water via piezoelectric-assisted visible-light photocatalysis of CdS nanorod arrays, *ChemCatChem* 10 (2018) 3397–3401.
- [25] M. Zhang, S. Nie, T. Cheng, Y. Feng, C. Zhang, L. Zheng, L. Wu, W. Hao, Y. Ding, Enhancing the macroscopic polarization of CdS for piezo-photocatalytic water splitting, *Nano Energy* 90 (2021), 106635.
- [26] X. Wang, Y. Zhang, H. Si, Q. Zhang, J. Wu, L. Gao, X. Wei, Y. Sun, Q. Liao, Z. Zhang, K. Ammarah, L. Gu, Z. Kang, Y. Zhang, Single-atom vacancy defect to trigger high-efficiency hydrogen evolution of MoS₂, *J. Am. Chem. Soc.* 142 (2020) 4298–4308.
- [27] C. Du, Q. Zhang, Z. Lin, B. Yan, C. Xia, G. Yang, Half-unit-cell ZnIn₂S₄ monolayer with sulfur vacancies for photocatalytic hydrogen evolution, *Appl. Catal. B* 248 (2019) 193–201.
- [28] D. Lang, Q. Xiang, G. Qiu, X. Feng, F. Liu, Effects of crystalline phase and morphology on the visible light photocatalytic H₂ production activity of CdS nanocrystals, *Dalton Trans.* 43 (2014) 7245–7253.
- [29] C. Hu, F. Chen, Y. Wang, N. Tian, T. Ma, Y. Zhang, H. Huang, Exceptional cocatalyst-free photo-enhanced piezocatalytic hydrogen evolution of carbon nitride nanosheets from strong in-plane polarization, *Adv. Mater.* 33 (2021), 2101751.
- [30] Y. Wang, D. Chen, L. Qin, J. Liang, Y. Huang, Hydrogenated ZnIn₂S₄ microspheres: boosting photocatalytic hydrogen evolution by sulfur vacancy engineering and mechanism insight, *Phys. Chem. Chem. Phys.* 21 (2019) 25484–25494.
- [31] S.A. Shah, G. Zhu, X. Shen, L. Kong, Z. Ji, K. Xu, H. Zhou, J. Zhu, P. Song, C. Song, A. Yuan, X. Miao, Controllable sandwiching of reduced graphene oxide in hierarchical defect-rich MoS₂ ultrathin nanosheets with expanded interlayer spacing for electrocatalytic hydrogen evolution reaction, *Adv. Mater. Interf.* 5 (2018), 1801093.
- [32] Y. Li, L. Ding, Z. Liang, Y. Xue, H. Cui, J. Tian, Synergetic effect of defects rich MoS₂ and Ti₃C₂ MXene as cocatalysts for enhanced photocatalytic H₂ production activity of TiO₂, *Chem. Eng. J.* 383 (2020), 123178.
- [33] M. Liu, C. Zhang, J. Su, X. Chen, T. Ma, T. Huang, A. Yu, Propelling polysulfide conversion by defect-rich MoS₂ nanosheets for high-performance Lithium-sulfur batteries, *ACS Appl. Mater. Interf.* 11 (2019) 20788–20795.
- [34] B. Chen, Y. Huang, Q. Zhang, D.D. Dionysiou, L. Wang, J. Li, Formation of nitrite and hydrogen peroxide in water during the vacuum ultraviolet irradiation process: impacts of pH, dissolved oxygen, and nitrate concentration, *Environ. Sci. Technol.* 55 (2021) 1682–1689.
- [35] J. Wang, C. Hu, Y. Zhang, H. Huang, Engineering piezoelectricity and strain sensitivity in CdS to promote piezocatalytic hydrogen evolution, *Chin. J. Catal.* 43 (2022) 1277–1285.
- [36] J. Zhang, S. Wageh, A. Al-Ghamdi, J. Yu, New understanding on the different photocatalytic activity of wurtzite and zinc-blende CdS, *Appl. Catal. B* 192 (2016) 101–107.
- [37] X. Zhou, F. Yan, S. Wu, B. Shen, H. Zeng, J. Zhai, Remarkable piezophoto coupling catalysis behavior of BiOX/BaTiO₃ (X = Cl, Br, Cl_{0.166}Br_{0.834}) piezoelectric composites, *Small* 16 (2020), 2001573.
- [38] J. Hu, Y. Chen, Y. Zhou, L. Zeng, Y. Huang, S. Lan, M. Zhu, Piezo-enhanced charge carrier separation over plasmonic Au-BiOBr for piezo-photocatalytic carbamazepine removal, *Appl. Catal., B* 311 (2022), 121369.
- [39] X. Zhang, P. Ma, C. Wang, L. Gan, X. Chen, P. Zhang, Y. Wang, H. Li, L. Wang, X. Zhou, K. Zheng, Unraveling the dual defect sites in graphite carbon nitride for ultra-high photocatalytic H₂O₂ evolution, *Energy Environ. Sci.* 15 (2022) 830–842.
- [40] J. Gao, H.B. Yang, X. Huang, S.-F. Hung, W. Cai, C. Jia, S. Miao, H.M. Chen, X. Yang, Y. Huang, T. Zhang, B. Liu, Enabling direct H₂O₂ production in acidic media through rational design of transition metal single atom catalyst, *Chem* 6 (2020) 658–674.
- [41] Z. Cai, L. Li, Y. Zhang, Z. Yang, J. Yang, Y. Guo, L. Guo, Amorphous nanocages of Cu-Ni-Fe hydr(oxy)oxide prepared by photocorrosion for highly efficient oxygen evolution, *Angew. Chem. Int. Ed.* 58 (2019) 4189–4194.
- [42] J. Kang, X. Qiu, Q. Hu, J. Zhong, X. Gao, R. Huang, C. Wan, L. Liu, X. Duan, L. Guo, Valence oscillation and dynamic active sites in monolayer nico-hydroxides for water oxidation, *Nat. Catal.* 4 (2021) 1050–1058.